



# Nitric oxide gas delivery by fluorinated poly(ethylene glycol)@graphene oxide carrier towards pharmacotherapeutics

Yitayal Admassu Workie, S Sabrina, Toyoko Imae, Marie Pierre Krafft

## ► To cite this version:

Yitayal Admassu Workie, S Sabrina, Toyoko Imae, Marie Pierre Krafft. Nitric oxide gas delivery by fluorinated poly(ethylene glycol)@graphene oxide carrier towards pharmacotherapeutics. ACS Biomaterials Science and Engineering, 2019, 10.1021/acsbiomaterials.9b00474 . hal-03018428

**HAL Id: hal-03018428**

**<https://hal.science/hal-03018428>**

Submitted on 22 Nov 2020

**HAL** is a multi-disciplinary open access archive for the deposit and dissemination of scientific research documents, whether they are published or not. The documents may come from teaching and research institutions in France or abroad, or from public or private research centers.

L'archive ouverte pluridisciplinaire **HAL**, est destinée au dépôt et à la diffusion de documents scientifiques de niveau recherche, publiés ou non, émanant des établissements d'enseignement et de recherche français ou étrangers, des laboratoires publics ou privés.

# Nitric oxide gas delivery by fluorinated poly(ethylene glycol)@graphene oxide carrier towards pharmacotherapeutics

Yitayal Admassu Workie,<sup>†</sup> Sabrina,<sup>‡</sup> Toyoko Imae,<sup>†,‡,\*</sup> and Marie Pierre Krafft<sup>§</sup>

<sup>†</sup>Graduate Institute of Applied Science and Technology, National Taiwan University of Science and Technology, Taipei 10607, Taiwan

<sup>‡</sup>Department of Chemical Engineering, National Taiwan University of Science and Technology, Taipei 10607, Taiwan

<sup>§</sup>University of Strasbourg, Charles Sadron Institute (CNRS), 23 rue du Loess. 67034 Strasbourg, France

Corresponding authors E-mail:

+886227303627 [imaie@mail.ntust.edu.tw](mailto:imaie@mail.ntust.edu.tw) (T. I.),

## ABSTRACT

In view of preparing effective nitric oxide gas carriers, a fluorinated poly(ethylene glycol) (*F*-PEG) was non-covalently conjugated with acid-treated graphene oxide (GO) to prepare the composite of *F*-PEG@GO. When the persistence of NO gas doped on GO and *F*-PEG@GO was investigated for 3 h, the conserved NO gas decreased from 49.00±7.06 to 2.17±1.36 nmol/mg carrier and from 58.51± 6.02 to 4.58±2.22 nmol/mg carrier, respectively. The adsorption of *F*-PEG on GO and the doping of NO on GO and *F*-PEG@GO were declarative by the increase of distance between GO sheets, and the NO-doping was also clarified by infrared absorption and X-ray photoelectron spectroscopies. The anti-bacterial effect was higher for NO-conserved *F*-PEG@GO than for NO-conserved GO and more effective against *Staphylococcus aureus* than against *Escherichia coli*. It is evident that the coating of *F*-PEG on GO is preferable for advancing the loading efficiency, the stability and the biomedical efficacy of NO gas.

**Keywords:** Nitric oxide; Graphene oxide; Fluorinated poly(ethylene glycol); Anti-bacterial activity; Escherichia coli; Staphylococcus aureus.

## INTRODUCTION

Nitric oxide (NO), is known to have vasodilator, tumoricidal and antibacterial properties.<sup>1</sup> The pharmacotherapeutic effect of NO has been proven by its concentration-dependence and high reactivity.<sup>2</sup> In response to the needs for bioactive molecules in therapy, some works have been done on the synthesis of NO donor with prodrug concept: Though several NO donors were reported like N-diazeniumdiolate,<sup>3</sup> S-nitrosothiol,<sup>4</sup> transition-metal nitrosyl complexes and alkyl nitrites,<sup>5</sup> there is scarce work on developing novel material that can be an efficient scaffold to store gaseous NO and deliver it to the target localization.

Graphene oxide (GO) is a sheet of carbon atoms bonded into a two-dimensional honeycomb lattice,<sup>6</sup> which has carboxylic, phenol and epoxide groups at its defected edges.<sup>7</sup> Due to the richness of oxidized functional groups, GO has a possibility of many biomedical applications including drug delivery,<sup>8,9</sup> biosensing<sup>10</sup> and bioimaging.<sup>11</sup> In order to increase the biocompatibility and water dispersibility, GO was hybridized with hydrophilic polymers like polyethylene glycol<sup>12</sup>, sugar based polymers,<sup>13,14</sup> and poly(amido amine).<sup>9</sup> Fluorocarbons are excellent media of gases, in particular, of respiratory gases, due to their low intermolecular van der Waals interactions.<sup>15</sup> For this reason, they can be used as oxygen carriers, when they form emulsions.<sup>16-18</sup> Because fluorinated carbon materials may be one of the most promising carriers of gases like oxygen for biological treatments,<sup>19</sup> the binding of fluorinated poly(ethylene glycol) (*F*-PEG) on GO will be valuable as gaseous drug delivery systems with improved biocompatibility.

In the present work, *F*-PEG-coated GO nanocomposite platform was prepared as a novel material for NO gas delivery system. Hybridization of *F*-PEG on the surface of GO was expected to heighten the doping of the NO gas for exogenous delivery methods. The loading and self-release efficiencies of *F*-PEG@GO composites for NO gas were determined using Griess assay methods and compared with those of GO. The anti-bacterial activities of carried NO on GO and *F*-PEG@GO were examined against *Escherichia coli* and *Staphylococcus aureus*.

## EXPERIMENTAL

### Materials and methods

Natural graphite flake of 4  $\mu\text{m}$  size was obtained from Ito graphite Co. Ltd, Japan. Copper metal was purchased from Jianyuan Metal, Taiwan. Fluorinated polyethylene glycol derivative (*F*-PEG) ( $\text{F}_8\text{H}_5\text{COOPEG}_{5000}$ ) was synthesized by esterification of  $\text{F}_8\text{H}_5\text{COOH}$  and  $\text{CH}_3(\text{OCH}_2\text{CH}_2)_{5000}\text{OH}$ . Other chemicals were of commercial grade. All the reagents were used as received. Ultrapure water (resistivity of  $18.2 \text{ M}\Omega\text{cm}^{-1}$ , Yamato Millipore WT100) were used throughout the experimental work.

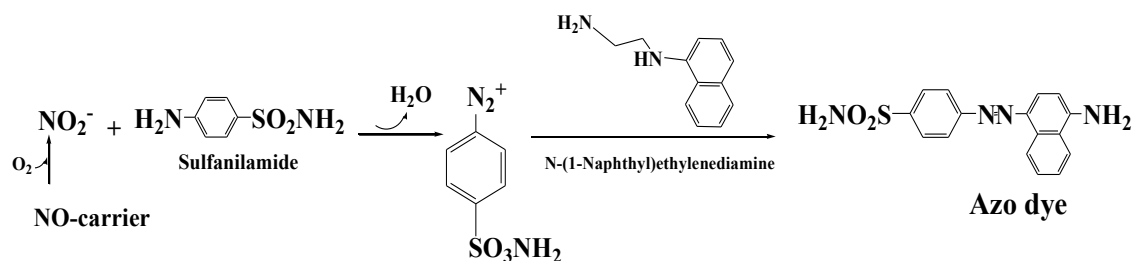
Characterization was performed using a transmission electron microscope (TEM, JEOL, Japan, 120 kV), a ultraviolet (UV)/Visible absorption spectrophotometer (UV-visible, JASCO V-670, Japan), a Fourier transform infrared absorption spectrophotometer (FTIR, NICOLET 6700, Thermo Scientific, USA), a thermogravimetric analysis (TGA, TA Q500, USA), a dynamic light scattering (DLS, SZ-100, HORIBA scientific, Japan), an X-ray diffractometer (Bruker, D2 Phaser, USA), a Raman scattering spectrometer (Horiba Jobin Yvon iHR550, Japan) and a X-ray photoelectron spectrometer (XPS, VG Scientific, ESCALAB 250, England).

### Preparation of *F*-PEG@GO composites

GO sheets were prepared using the modified Hummers method from natural graphite flakes.<sup>20</sup> In brief, graphite flake (2.0 g) was acid-treated and exfoliated by mixing with sulfuric acid (98 %, 50 ml), sodium nitrate (2.0 g) and potassium permanganate (6.0 g), heating at 35 °C for one day, adding water (80 ml) and H<sub>2</sub>O<sub>2</sub> (30 %, 20 ml). The product was separated from supernatant by centrifugation (for 20 min at 6000 rpm). The precipitate was washed with an aqueous HCl solution and water until the pH of the supernatant became neutral and dried in vacuum oven overnight. For fragmentation, graphene oxides (20 mg) were ultrasonicated in water (40 ml, 0.5 mg/ml) for 4 h using a homogenizer (QSONICA Sonicator, Q700, Misonix, USA, amplitude intensity 50 and applied power 50 W) in an ice bath. The concentration of produced graphene oxide was determined from the calibration curve. *F*-PEG@GO composites were prepared by mixing equal volumes of graphene oxide in aqueous dispersion (300 µg/ml) and *F*-PEG in aqueous solution (24 µg/ml) and sonicating for 4 h. Then the weight ratio of *F*-PEG:GO in *F*-PEG@GO was 0.083:1.

### **Quantitative determination of doped NO gas by Griess assay method**

NO gas generated by reacting aqueous nitric acid with copper metal was continuously taken into the carrier materials (GO and *F*-PEG@GO) in the closed system. NO gas doped in carrier materials was measured using the universal Griess assay method with an affordable instrumentation and conceptually a straightforward analysis procedure.<sup>21</sup> As presented in the reaction [scheme 1](#), the principle of the measurement is the reactivity of NO in the formation of nitrite in oxygenated aqueous media<sup>22</sup> via the reaction with sulfanilamide under the acidic condition to form a diazonium salt intermediate. The diazonium salt intermediate is then coupled to *N*-1-naphthylethylenediamine dihydrochloride to form the stable water-soluble azo dye, which has an absorption band at  $\lambda_{\text{max}} \approx 540 \text{ nm}$ .<sup>23</sup>



Scheme 1. Reactions involved in the formation of an azo dye by coupling of diazonium salt of sulfanilamide and N-1-naphthylethylenediamine dihydrochloride.

A stock solution of sodium nitrate (0.01 M) was prepared by dissolving sodium nitrite (17.25 mg) in water (25 ml). N-1-naphthylethylenediamine dihydrochloride (25 mg) was dissolved into water (25 ml) to be a stock solution (0.1 %). Sulfanilamide (250 mg, 1 %) and phosphoric acid (1.25 ml, 5 %) was dissolved in water (25 ml). To plot a calibration curve of sodium nitrite, a series of solutions were prepared by taking 2.25 to 11.25  $\mu\text{l}$  (with an interval of 2.25  $\mu\text{l}$ ) from a stock solution of sodium nitrite (0.01 M) and 50  $\mu\text{l}$  of both sulfanilamide and N-1-naphthylethylenediamine dihydrochloride and the resulting solution were further dissolved in 1.5 ml of water. The calibration curve was prepared from the absorbance of the pink-colored solution at 540 nm.

The NO-doped carrier materials (10 mg) were dispersed in water (14 ml) and filtered out. For the filtrate (1 ml), 150  $\mu\text{l}$  of both sulfanilamide and N-1-naphthylethylenediamine dihydrochloride were added. Then the nitrite concentration was determined by comparing the absorbance of the pink-colored azo dye solution at 540 nm to a calibration curve prepared with known concentrations of nitrite, and thus the amount of NO on carrier was determined stoichiometrically.

### Antibacterial activity test

The anti-bacterial test was done based on the standard agar disk-diffusion method.<sup>24</sup> Aerobically grown *E. coli* (gram negative) and *S. aureus* (gram positive) strain suspensions (100  $\mu$ l) with optical density 0.05 were spread evenly over the face of a sterile plate grown in luria bertani and tryptone soya broth agar medium, respectively. Equal amounts of GO and *F*-PEG@GO were applied as controls (non-NO doped) and tests (NO doped) on the surface of agar plate cultured with *E. coli* and *S. aureus* by incubated for 12-16 h.

## Results and Discussion

### Characterization of Composites

*F*-PEG@GO composite was prepared by mixing GO with *F*-PEG. TEM images were taken for GO and *F*-PEG@GO and their morphologies were compared in Fig.1: In contrast to thin GO sheets with lateral dimensions ranged around hundred nm, a TEM image of *F*-PEG@GO displayed the dense density of GO sheet, suggesting the adsorption of *F*-PEG. It has been reported that the binding and covering of poly(propylene fumarate)/poly(ethyl glycol) derivative on the surface GO sheet causes to increase the size.<sup>25</sup> Averaged particle sizes of *F*-PEG, GO and *F*-PEG@GO in water were measured by dynamic light scattering. While the average hydrodynamic size of *F*-PEG was 1,098 nm, GO and *F*-PEG@GO showed values of 207 and 250 nm, respectively. The large size of *F*-PEG indicates the aggregation of *F*-PEG. Different from such situation, when *F*-PEG was mixed with GO, the size of *F*-PEG@GO was only slightly larger than it of GO and large aggregates of *F*-PEG alone were not observed. The drastic size variation between *F*-PEG and *F*-PEG@GO suggests the enough adsorption of *F*-PEG on GO and the formation of the complex.

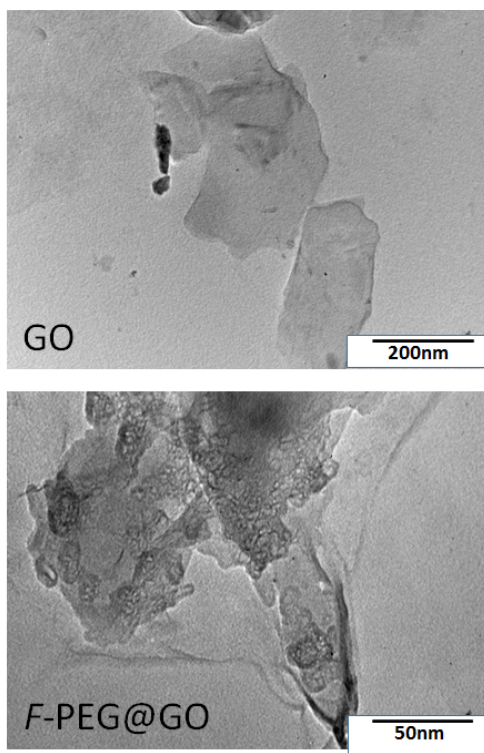


Fig. 1. TEM images of GO and *F*-PEG@GO.

FTIR spectra of *F*-PEG, GO and *F*-PEG@GO are shown in Fig. 2A. An FTIR spectrum of *F*-PEG showed bands of O-H(H<sub>2</sub>O) stretching (3430 cm<sup>-1</sup>), alkane CH<sub>2</sub> stretching (2914 cm<sup>-1</sup>), O-H(H<sub>2</sub>O) bending (1640 cm<sup>-1</sup>), CH<sub>2</sub> scissor (1460 cm<sup>-1</sup>), CH<sub>2</sub> wagging (1350 cm<sup>-1</sup>), CH<sub>2</sub> twisting (1258 cm<sup>-1</sup>) and C-F stretching (1110 cm<sup>-1</sup>). GO contains the absorption bands of O-H (3380 cm<sup>-1</sup>), carbonyl C=O (1730 cm<sup>-1</sup>), aromatic C=C (1630 cm<sup>-1</sup>), O-H bending (1360 cm<sup>-1</sup>), aromatic C-C (1220 cm<sup>-1</sup>), and alkoxy C-O-C (1050 cm<sup>-1</sup>) groups.<sup>26</sup> The appearance of oxygen-containing functional groups confirmed the preparation of GO. Meanwhile, *F*-PEG@GO composite had characteristic IR bands of both *F*-PEG and GO; CH<sub>2</sub> stretching (2880 cm<sup>-1</sup>) and C-F stretching (1110 cm<sup>-1</sup>) from *F*-PEG and carbonyl C=O (1730 cm<sup>-1</sup>) from GO were noticeably observed in the composite, indicating the coexistence of *F*-PEG and GO in *F*-PEG@GO.



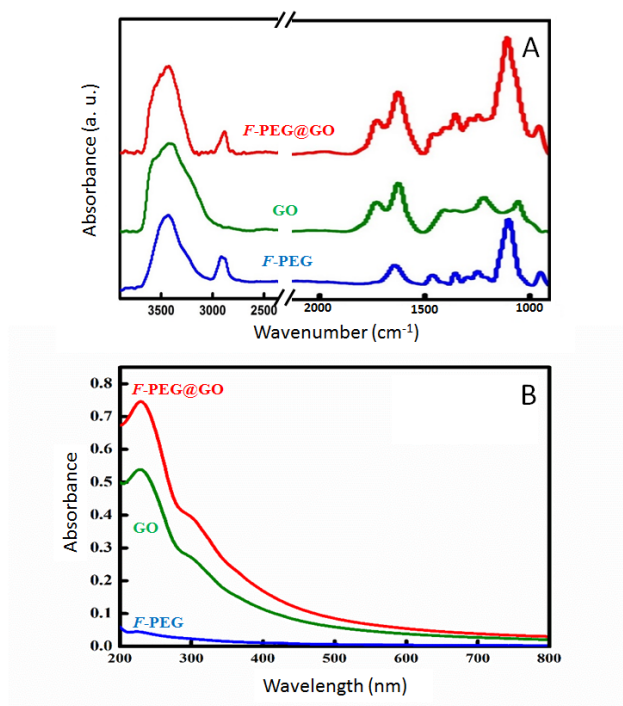


Fig. 2. (A) FTIR absorption spectra and (B) UV-visible absorption spectra of *F*-PEG, GO, and *F*-PEG@GO.

Fig. 2B presents the UV-visible absorption spectra of *F*-PEG, GO and *F*-PEG@GO. Although *F*-PEG did not show any absorption band in the region of 200 to 800 nm, GO displayed a main band at 230 nm and a shoulder band around 300 nm, which correspond to a  $\pi$ - $\pi^*$  and  $n$ - $\pi^*$  electronic transition modes, respectively.<sup>26</sup> Same bands were observed even for *F*-PEG@GO and thus no variation happened on UV-visible absorption bands after adsorption of *F*-PEG on GO, indicating that *F*-PEG on the surface of GO does not affect the electron transition state of GO.<sup>8</sup>

TGA curves of GO and *F*-PEG@GO were compared as presented in Fig. 3. While graphite possessed high thermal stability at the range from 25 to 650 °C and was completely decomposed at 980 °C,<sup>27</sup> GO displayed 8 % loss of its mass below 100 °C, due to the evaporation of adsorbed water and small molecules. The first decomposition occurred below 200 °C and lost about 29 %

of the mass. Additional decomposition of about 15 % happened below 320 °C. The remaining mass loss (about 48 %) started at 475 °C. Oxygen-including moieties should be burned in early stages and the elimination of the graphene moiety could be at the last stage but at the lower temperature than that of graphite. Thermogram of *F*-PEG@GO composite showed the thermal decomposition pattern of the 4 % mass lost below 100 °C as a result of the evaporation of absorbed water and small molecules. The weight losses of *F*-PEG@GO happened at two steps of about 46% loss and the remaining about 50% loss. However, these losses occurred at higher temperatures (about 27 °C) than those of GO, and the final decomposition was at 580 °C.<sup>25</sup> The temperature rise of the final decomposition is because of the heat-generated aromatization in *F*-PEG@GO.<sup>28</sup>

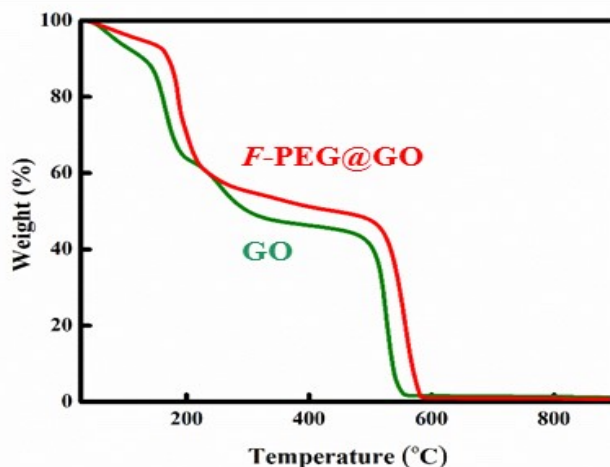


Fig .3. TGA charts of GO and *F*-PEG@GO.

The XRD patterns of graphite, *F*-PEG, GO and *F*-PEG@GO were presented in Fig. 4. While an X-ray diffractogram of graphite, the highly ordered carbon material, appeared a sharp diffraction peak (002) at  $2\theta = 26.60^\circ$  of hexagonal crystalline structure (JPCDS No 89-8487),<sup>27,29</sup> an (001) peak of GO (hexagonal crystalline structure, JPCDS No 46-1628) at  $11.40^\circ$  confirmed the formation of graphene oxide. *F*-PEG displayed two major peaks at  $19.05^\circ$  and  $23.30^\circ$  and weak

peaks at  $14.69^\circ$  and  $26.18^\circ$ , which were indexed to (120), ( $\bar{1}31$ ), (021) and ( $\bar{2}24$ ), respectively, of monoclinic crystalline structure (JPCDS No 52-2279).<sup>25</sup> However, the addition of *F*-PEG on GO arose a strong peak to diffract at  $9.14^\circ$  and a weak peak at  $18.40^\circ$  assigned to (001) and (002), respectively, of hexagonal crystalline structure (JPCDS No 53-1791).<sup>30</sup> These results indicate the strong adsorption of *F*-PEG on GO enough to perturb the crystallography of each component.

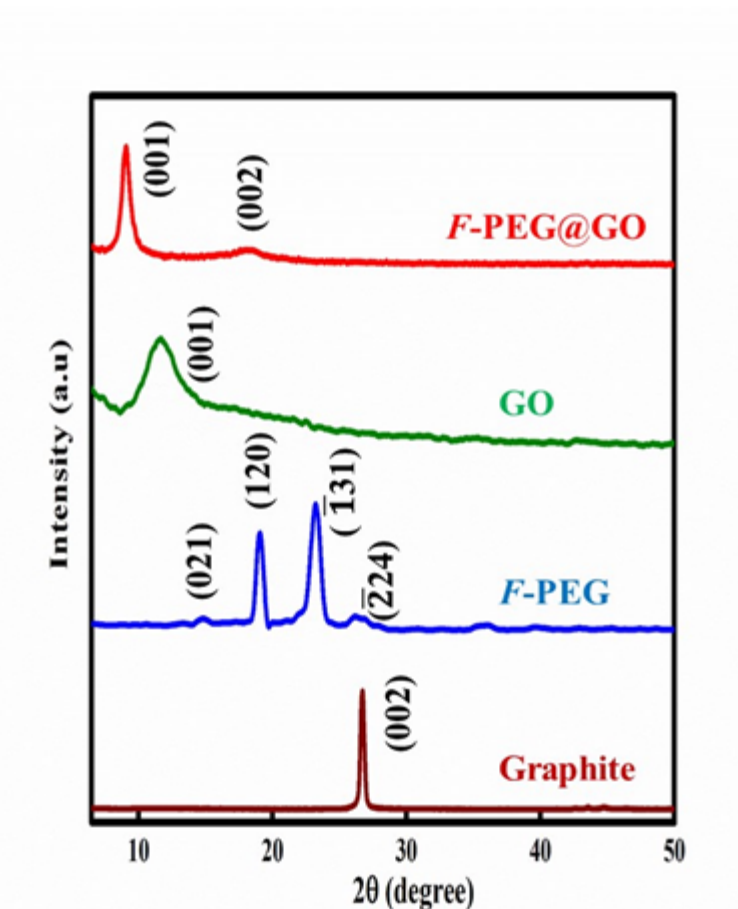


Fig. 4. XRD patterns of graphite, *F*-PEG, GO and *F*-PEG@GO.

Fig. 5 presents the Raman spectra of graphite, *F*-PEG, GO and *F*-PEG@GO. For *F*-PEG, bands appeared at  $2936\text{ cm}^{-1}$  was assigned to stretching vibration mode of alkyl chain. The  $\text{CH}_2$  scissoring, wagging and twisting bands were found at  $1471\text{ cm}^{-1}$ ,  $1271\text{ cm}^{-1}$ , and  $1225\text{ cm}^{-1}$ , respectively. A band at  $1132\text{ cm}^{-1}$  attributed to C-F stretching mode and the C-O-C stretching

vibration band was observed at  $1055\text{ cm}^{-1}$ . A band at  $835\text{ cm}^{-1}$  was assigned to carbon skeleton of *F*-PEG.<sup>31</sup> While graphite had three Raman bands: A G-band ( $\text{sp}^2$ ) and a weak D-band ( $\text{sp}^3$ ) appeared at  $1581$  and  $1326\text{ cm}^{-1}$  and the 2D band was observed at  $2689\text{ cm}^{-1}$ ,<sup>32</sup> in GO, the appearance of a D-band at  $1333\text{ cm}^{-1}$  besides a G-band at  $1601\text{ cm}^{-1}$  confirms the partial defect of graphitic structure in GO. Then, the G-band and D-band ( $1598$  and  $1327\text{ cm}^{-1}$ , respectively) of *F*-PEG@GO were scarcely changed, as compared to GO.<sup>33</sup> Non covalent binding of *F*-PEG on GO may cause the scarce variation on the vibration state.

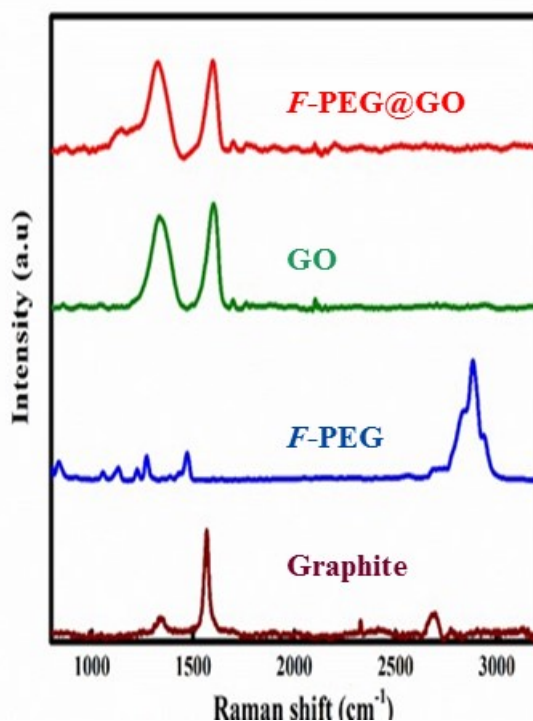


Fig. 5. Raman spectra of graphite, *F*-PEG, GO and *F*-PEG@GO.

### Doping of NO gas

The loading efficiency of NO in carriers was evaluated: The loaded amount of NO after 5 min was  $58.51 \pm 6.02\text{ mmol/g}$  for *F*-PEG@GO carrier and  $49.00 \pm 7.06\text{ mmol/g}$  for GO carrier. However, the loaded NO in both carriers decreased with time in air atmosphere and thus it came down to

$4.58 \pm 2.22$  and  $2.17 \pm 1.36$  mmol/g(carrier), respectively, after 3 h, As seen in Fig. 6. This phenomenon may happen by the reasons that NO was probably oxidized to NO<sub>2</sub> by coexisting oxygen or released from the carrier. Thus, it was confirmed that GO can load NO but the coating of *F*-PEG on the surface of GO enhanced the trapping ability of NO gas on the carrier. Moreover, the reservation of NO gas on carriers was only 8 % for *F*-PEG@GO and 4 % for GO.

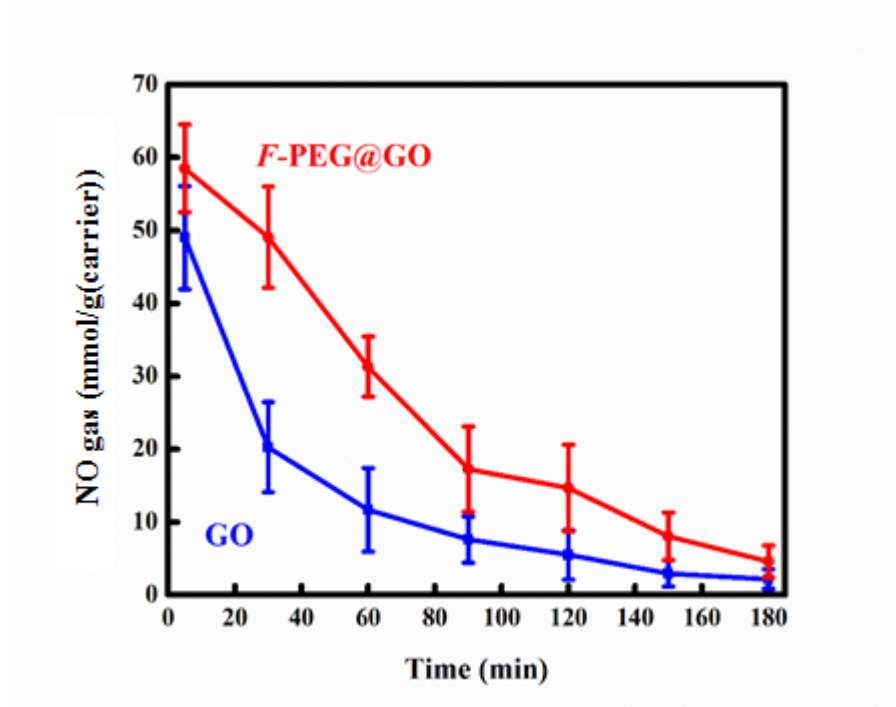


Fig. 6. NO gas reserved in GO and *F*-PEG@GO carriers.

After NO gas was doped on GO and *F*-PEG@GO, FTIR absorption spectra were compared with those of carriers before NO-doping. As seen in Fig. 7A(a), even after NO was doped, intrinsic absorption bands of both GO and *F*-PEG@GO were conserved, except the appearance of a strong band at  $1384\text{ cm}^{-1}$ , which may be attributed to a NO-relating vibration mode. This result confirmed the proper loading of NO in GO and *F*-PEG@GO carriers. Fig. 7A(b) displays FTIR absorption spectra of GO, which was NO-doped and leaved without additional doping for adequate time indicated in the figure. A band at  $1384\text{ cm}^{-1}$  decreased with the leaving and the diminution was

calculated as an intensity ratio of a band at  $1384\text{ cm}^{-1}$  against intensity of a band at  $1630\text{ cm}^{-1}$ , where a band intensity at  $1384\text{ cm}^{-1}$  was subtracted the contribution of intrinsic GO band. Then the ratio 2.4 at 10 min decreased to 1.4 after 120 min. This tendency is consistent with the decrease of NO in Fig. 6.

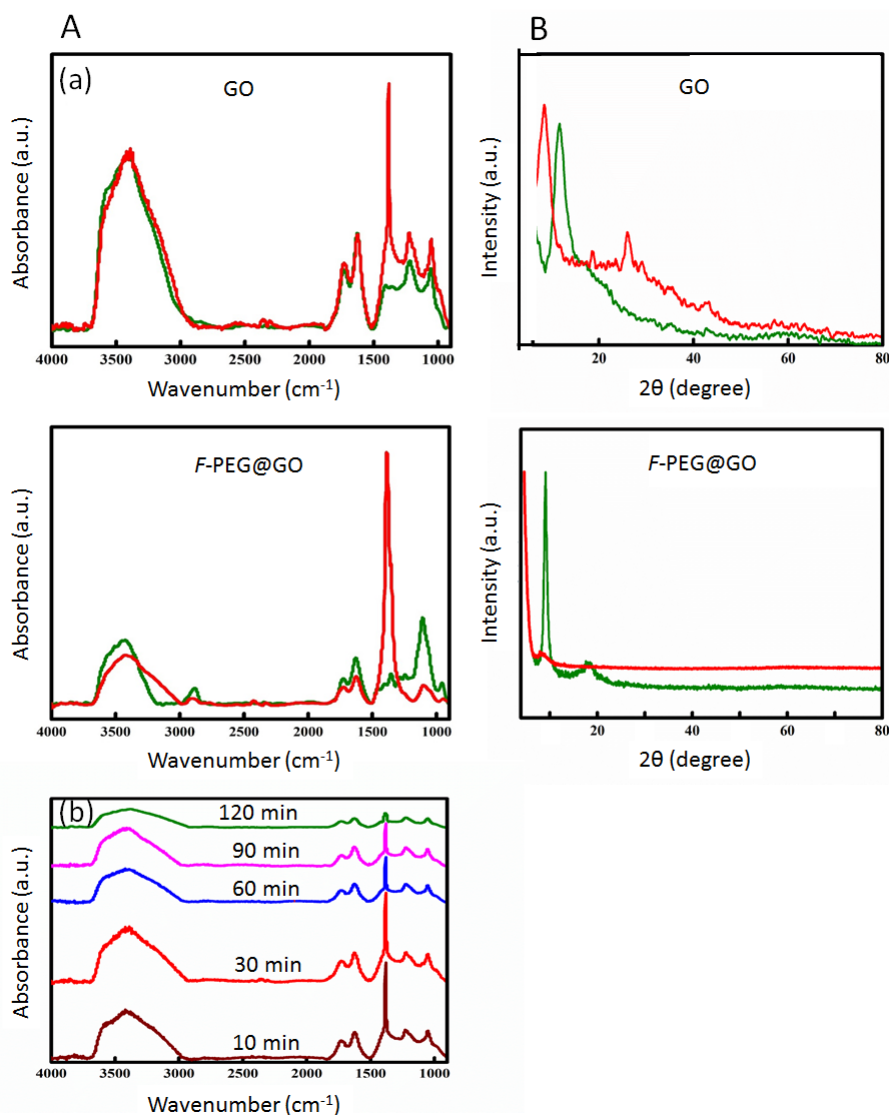
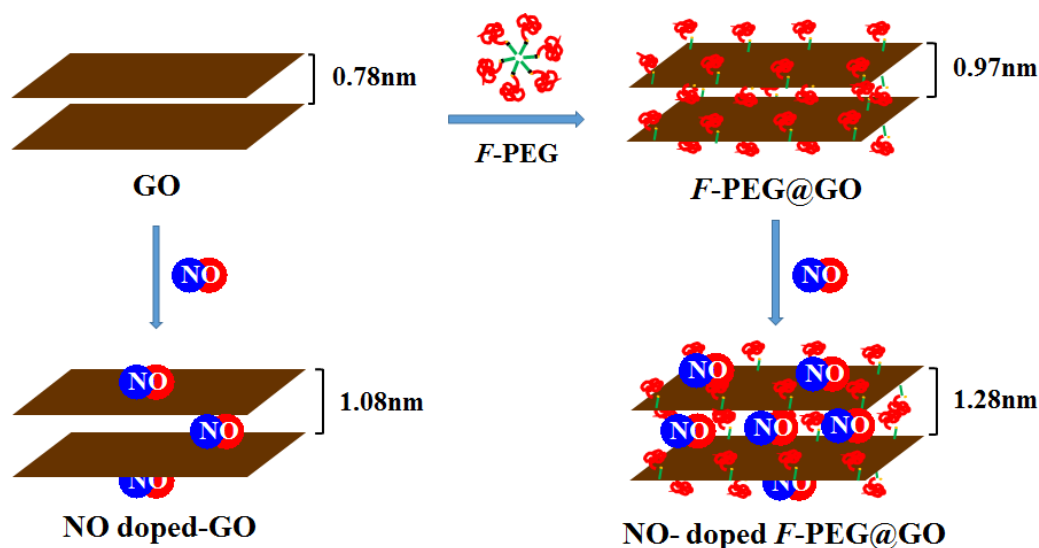


Fig. 7. (A)(a) FTIR absorption spectra and (B) XRD patterns of GO and *F*-PEG@GO. Green: NO-nondoped, red: NO-doped. (A)(b) FTIR absorption spectra of NO-doped GO. Time indicates after NO-doped.

The effect of NO-doping on the crystalline structure of GO and *F*-PEG@GO was also investigated as presented in Fig. 7B. The (001) diffraction peak of GO was shifted to low angle by  $3.20^\circ$  from its intrinsic peak position ( $11.40^\circ$ ) as a result of NO-doping. The (001) peak of *F*-PEG@GO were similarly changed from  $9.14^\circ$  to  $6.85^\circ$ , which were lowered angle by  $2.29^\circ$ . These shifts of (001) peaks correspond to 0.30 and 0.31 nm expansion of hexagonal layers after NO-doping in GO and *F*-PEG@GO, respectively. Considering to the space size (0.78 nm) between GO sheets, the space size (0.97 nm) after adsorption of *F*-PEG and molecular size (0.39 nm x 0.28 nm) of NO, the structures of GO, *F*-PEG@GO and their NO-doping states can be estimated as illustrated in Scheme 2. It was clearly shown that the crystalline structure of GO and *F*-PEG@GO were expanded due to the adsorption-induced deformation effect of NO gas.



Scheme 2 Schematic illustration of adsorption of *F*-PEG on GO and NO-doping on GO and *F*-PEG@GO.

The variation of chemical composition in GO and *F*-PEG@GO before and after NO-doping was assessed using XPS as shown in Fig. 8, where full XPS scan and fine analyses including their deconvolution are presented. The binding energy and the area intensity of deconvoluted peaks are



given in Table 1. Full XPS scan surveys were exhibited peaks that are assigned to C1s, N1s, O1s, and F1s. GO possessed deconvoluted C1s species of aromatic CC, carboxylic acid (COOH), ketone (C=O) and phenol (C-OH). *F*-PEG@GO showed additional alkyl (CH<sub>2</sub>) and carbon-fluorine (C-F) species contributed from *F*-PEG. O1s fine analysis appeared chemical species of ketone (C=O), carboxylic acid (C=O and OH) and phenol (OH) in GO. On the other hand, *F*-PEG@GO showed an additional species of ether (COC) from *F*-PEG but the binding energies of ester (C=O and C-O) were overlapped on binding energies of species from GO. Another characteristic of *F*-PEG@GO different from GO was the existence of F1s originated from CF<sub>2</sub> and CF<sub>3</sub> in *F*-PEG. The existence of these species was consistent with the results from FTIR and Raman spectra.

Essentially, similar binding energies and area intensities were obtained for species of GO besides additional species from *F*-PEG even after the binding of *F*-PEG and, moreover, the binding species and their energies of GO and *F*-PEG@GO were not significantly changed after NO-doping. These results imply that the chemical state of GO was not affected by non-covalent functionalization by *F*-PEG, being coincided with the result of electronic state from UV-visible absorption spectra.

It should be noted that both NO-doped GO and *F*-PEG@GO provided chemical species of both NO and NO<sub>2</sub>: N1s fine analysis of GO and *F*-PEG@GO showed two species coming from NO<sup>34</sup> and NO<sub>2</sub>,<sup>35</sup> although O1s of NO and NO<sub>2</sub> indicated similar binding energies. Relatively higher area intensity of NO species in N1s of *F*-PEG@GO than those of NO<sub>2</sub> species in N1s of *F*-PEG@GO and NO species in N1s of GO may support the result of NO-loading in *F*-PEG@GO superior to GO as shown in Fig. 6. Coexisting NO<sub>2</sub> may be doped simultaneously with NO or oxidized from NO.



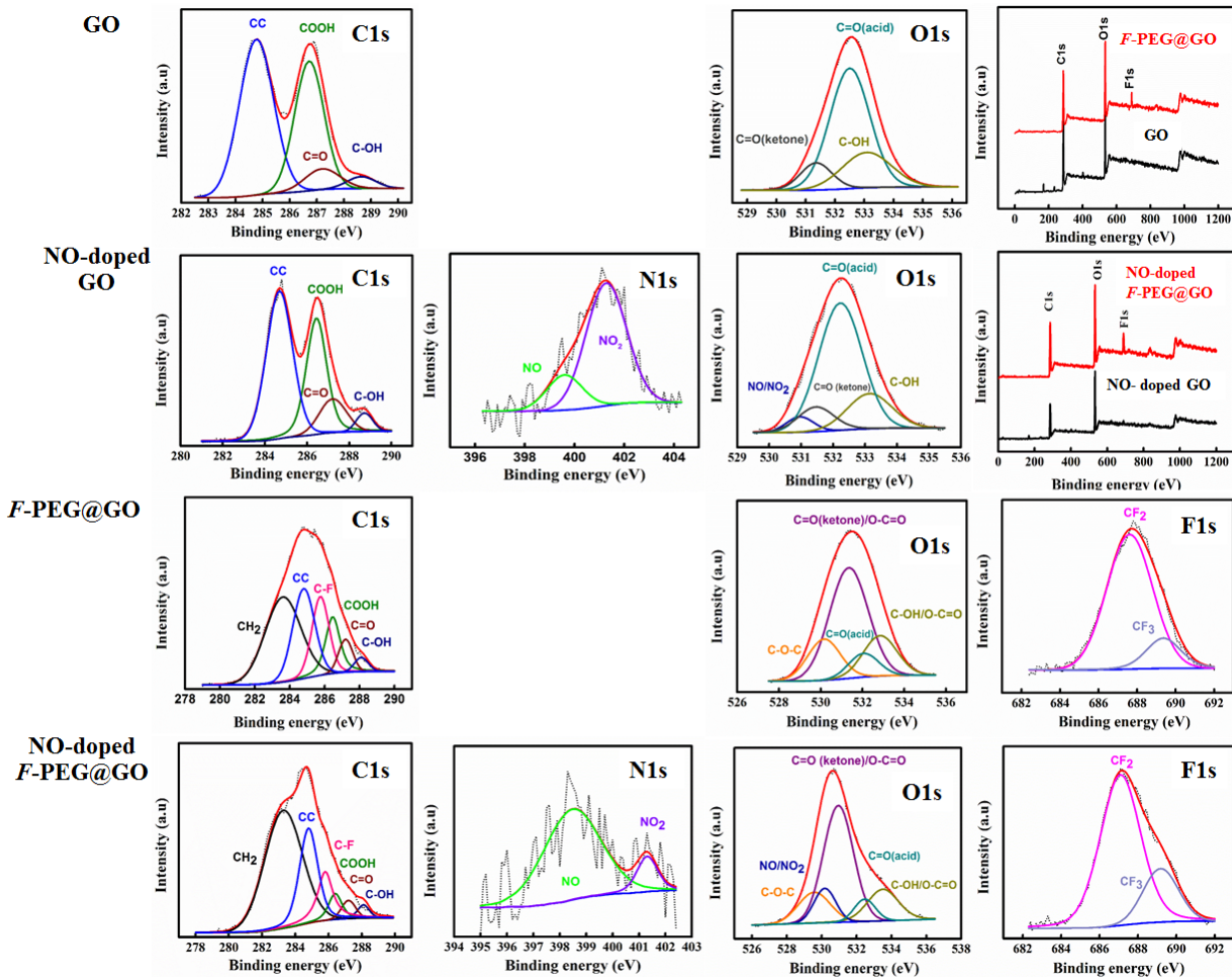


Fig. 8. XPS spectra and elemental deconvolution spectra of GO, *F*-PEG@GO, NO-doped GO, and NO-doped *F*-PEG@GO.

Table 1. Binding energy and area intensity from XPS spectra of GO, *F*-PEG@GO, NO-doped GO and NO-doped *F*-PEG@GO.

Element	GO		NO-doped GO		<i>F</i> -PEG@GO		NO-doped <i>F</i> -PEG@GO		Assignment
	BE (eV)	Area intensity	BE (eV)	Area intensity	BE (eV)	Area intensity	BE (eV)	Area intensity	
C1s					283.6	1735	283.6	2588	CH <sub>2</sub> *
	284.8	3463	284.8	1494	284.8	1120	284.8	1168	CC(aromatic)
					285.8	810	285.8	608	CF*
	286.7	2448	286.7	997	286.4	575	286.4	253	COOH(acid)
	287.2	472	287.2	342	287.2	262	287.2	148	C=O(ketone)

N1s	288.7	219	288.7	114	288.1	110	288.1	103	COH(phenol)
			399.5	30			399.5	64	NO**
			401.2	117			401.3	10	NO <sub>2</sub> **
O1s					530.1	1010	529.6	996	COC(ether)*
			530.9	200			530.3	479	NO**, NO <sub>2</sub> **
	531.4	991	531.4	448	531.4	3144	531.0	3540	C=O(ketone)
F1s									O-C=O(ester)*
	532.5	5433	532.5	2632	532.1	520	532.4	475	C=O(acid)
	533.1	1944	533.1	762	532.8	1033	533.5	1062	COH(acid, phenol)
									O-C=O(ester)*
F1s					687.7	882	687.1	1509	CF <sub>2</sub> *
					689.3	167	689.2	428	CF <sub>3</sub> *

\*, assignment to *F*-PEG. \*\*, assignment to NO or NO<sub>2</sub>.

### Anti-bacterial effect of NO doped on GO and *F*-PEG@GO

Following the reports that NO is known as a promising anti-bacterial agent,<sup>36</sup> the anti-bacterial activity of NO in GO and *F*-PEG@GO carriers was examined against gram negative and gram positive bacteria compared to control, as presented in Fig. 9. While the grown *E. coli* colonies were clearly visible on the control GO, the NO-doped GO showed the anti-bacterial activity towards *E. coli* (see Fig. 9A(a) and (c)). Similarly, the growth of *E. coli* colonies happened on the control of *F*-PEG@GO but NO-doped *F*-PEG@GO displayed significant anti-bacterial activity against *E. coli* with wider zone of inhibition than N-doped GO (see Fig. 9A(b) and (d)). Same tendency was observed even for *S. aureus*. As shown in Fig. 9B, control GO did not influence the growth of *S. aureus*, but the doping of NO on GO inhibited its growth (Fig. 9B(a) and (c)). Correspondingly, while control *F*-PEG@GO had no resistance on the growth of bacteria, NO-doped *F*-PEG@GO showed the observable conquest against pathogen with the higher zone of inhibition than NO-doped GO (Fig. 9B(b) and (d)). Moreover, it should be noted that NO was more effective for *S. aureus* than for *E. coli*. Similar result was reported previously.<sup>37</sup> NO-loading systems in the present work with anti-bacterial activity without chemical derivatization showed a

comparable conservation efficiency to the previously reported NO donors, N-diazeniumdiolate and S-nitrosothiol, with a principle of chemical variation in the carrier.<sup>38</sup>

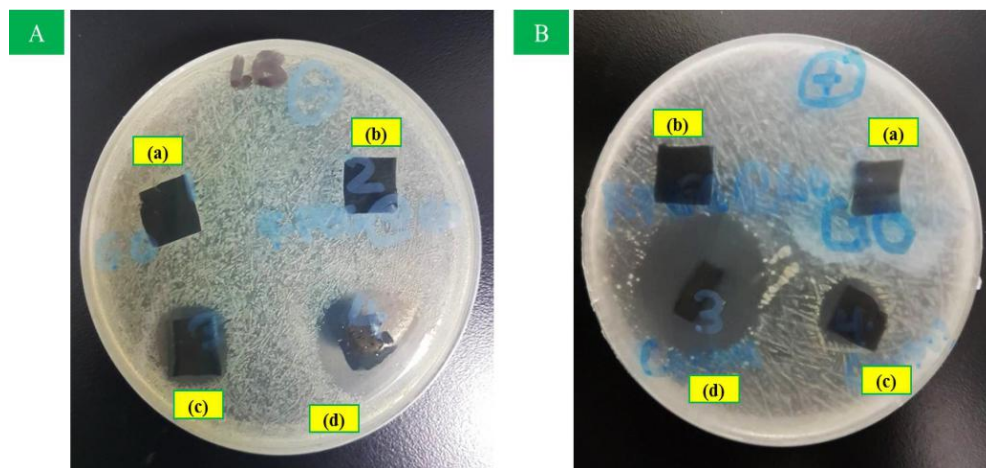


Fig. 9. Images after anti-bacterial test for (A) *E. coli* and (B) *S. aureus* on (a) control GO, (b) control *F*-PEG@GO (c) NO-doped GO and (d) NO-doped *F*-PEG@GO.

## CONCLUSIONS

The biomedical application of NO is consequently limited owing to the instability of the gas and the unavailability of the materials that were developed to encapsulate the gas. In this work, NO-preserving graphene-based platform and its composite with *F*-PEG were successfully prepared. The conserving efficiencies of the GO and *F*-PEG@GO were compared on the same time course framework. The efficiency may depend on the chemical structure and characteristics of NO carriers. Graphene was assumed to be familiar to NO-doping. The possible trial to increase the NO conservation is the creation of the hydrophobic domain possessing gas-encapsulating properties. Thus, the *F*-PEG-coated GO composite with hydrophobic perfluorocarbon moiety was effective for NO conservation superior to GO. Moreover, *F*-PEG@GO exerted the anti-bacteria effect than GO. However, the NO-conservation on these carriers showed the decreasing tendency

with time. This phenomenon should be the oxidation of NO to NO<sub>2</sub> rather than the release of NO from the carrier. Thus, the further invention is necessary for creating the conserved NO-protecting system.

## AUTHOR INFORMATION

### Corresponding Author

E-mail: [imae@mail.ntust.edu.tw](mailto:imae@mail.ntust.edu.tw)

Tel: +886-2-2730-3627

Notes

The authors declare no competing financial interest.

## ACKNOWLEDGEMENTS

This work was partially supported by a grant from the France/Taiwan Programme of Integrated Actions (PIA) Orchid. YAW gratefully acknowledge National Taiwan University of Science and Technology, Taiwan, for the financial support by a student scholarship. Authors also thank to Prof. C. K. Lee and Prof. M. Ujihara, National Taiwan University of Science and Technology, Taiwan, and Prof. Mounir Tarek, CNRS, France, for their valuable discussion and support. Authors also give a thank to Dr. M. M. M. Ahmed, Dr. C.-C. Chang, and Mr. J.-Y. Rao, National Taiwan University of Science and Technology, Taiwan, for their kind technical supports.

## REFERENCES

1. Shin, J. H.; Metzger, S. K.; Schoenfish, M. H. Synthesis of Nitric Oxide-Releasing Silica Nanoparticles. *J. Am. Chem. Soc.* **2007**, *129*, 4612-4619.
2. Friedman, A. J.; Han, G.; Navati, M. S.; Chacko, M.; Gunther, L.; Alfieri, A.; Friedman, J. M. Sustained release nitric oxide releasing nanoparticles: characterization of a novel delivery platform based on nitrite containing hydrogel/glass composites. *Nitric Oxide*. **2008**, *19* (1), 12-20.

3. Chakrapani, H.; Maciag, A. E.; Citro, M. L.; Keefer, L. K.; Saavedra, J. E. Cell-Permeable Esters of Diazeniumdiolate-Based Nitric Oxide Prodrugs. *Org. Lett.* **2008**, *22*, 5155-5158.
4. Lutzke, A.; Tapia, J. B.; Neufeld, M. J.; Reynolds, M. M. Sustained Nitric Oxide Release from a Tertiary S-Nitrosothiol-based Polyphosphazene Coating. *ACS Appl. Mater. Interfaces.* **2017**, *9* (3), 2104-2113.
5. Luo, R.; Liu, Y.; Yao, H.; Jiang, L.; Wang, J.; Weng, Y.; Zhao, A.; Huang, N. Copper-Incorporated Collagen/Catechol Film for in Situ Generation of Nitric Oxide. *ACS Biomater. Sci. Eng.* **2015**, *1* (9), 771-779.
6. Yu, H.; Zhang, B.; Bulin, C.; Li, R.; Xing, R. High-efficient Synthesis of Graphene Oxide Based on Improved Hummers Method. *Sci Rep.* **2016**, *6*, 36143.
7. Liu, S.; Zeng, T. H.; Hofmann, M.; Burcombe, E.; Wei, J.; Jiang, R.; Kong, J.; Chen, Y. Antibacterial Activity of Graphite, Graphite Oxide, Graphene Oxide, and Reduced Graphene Oxide: Membrane and Oxidative Stress. *ACS Nano.* **2011**, *5*, 6971-6980.
8. Chen, J.; Liu, H.; Zhao, C.; Qin, G.; Xi, G.; Li, T.; Wang, X.; Chen, T. One-step reduction and PEGylation of graphene oxide for photothermally controlled drug delivery. *Biomaterials.* **2014**, *35* (18), 4986-95.
9. Siriviriyannun, A.; Popova, M.; Imae, T.; Kiew, L. V.; Looi, C. Y.; Wong, W. F.; Lee, H. B.; Chung, L. Y. Preparation of graphene oxide/dendrimer hybrid carriers for delivery of doxorubicin. *Chem. Eng. J.* **2015**, *281*, 771-781.
10. Georgakilas, V.; Tiwari, J. N.; Kemp, K. C.; Perman, J. A.; Bourlinos, A. B.; Kim, K. S.; Zboril, R. Noncovalent Functionalization of Graphene and Graphene Oxide for Energy Materials, Biosensing, Catalytic, and Biomedical Applications. *Chem. Rev.* **2016**, *116* (9), 5464-519.

11. Nanda, S. S.; Papaefthymiou, G. C.; Yi, D. K. Functionalization of Graphene Oxide and its Biomedical Applications. *Crit. Rev. Solid State Mater. Sci.* **2015**, *40* (5), 291-315.
12. Kiew, S. F.; Kiew, L. V.; Lee, H. B.; Imae, T.; Chung, L. Y. Assessing biocompatibility of graphene oxide-based nanocarriers: A review. *J. Control Release.* **2016**, *226*, 217-228.
13. Hsu, Y. H.; Hsieh, H. L.; Viswanathan, G.; Voon, S. H.; Kue, C. S.; Saw, W. S.; Yeong, C. H.; Azlan, C. A.; Imae, T.; Kiew, L. V.; Lee, H. B.; Chung, L. Y. Multifunctional carbon-coated magnetic sensing graphene oxide-cyclodextrin nanohybrid for potential cancer theranosis. *J. Nanopart. Res.* **2017**, *19* (11). 359-378.
14. Kiew, S. F.; Ho, Y. T.; Kiew, L. V.; Kah, J. C. Y.; Lee, H. B.; Imae, T.; Chung, L. Y. Preparation and characterization of an amylase-triggered dextrin-linked graphene oxide anticancer drug nanocarrier and its vascular permeability. *Int. J. Pharm.* **2017**, *534* (1-2), 297-307.
15. Krafft, M. P.; Riess, J. G. Perfluorocarbons, life sciences and biomedical uses. *J. Polymer Sci. Part A: Polymer Chem.* **2007**, *45*, 1185-1198.
16. Krafft, M. P. Fluorocarbons and fluorinated amphiphiles in drug delivery and biomedical research. *Adv. Drug Deliv. Rev.* **2001**, *47*, 209-228.
17. Riess, J. G. Injectable oxygen carriers (blood substitutes) - Raison d'être, chemistry, and some physiology. *Chem. Rev.* **2001**, *101*, 2797-2920.
18. Haiss, F.; Jolivet, R.; Wyss, M. T.; Reichold, J.; Braham, N. B.; Scheffold, F.; Krafft, M. P.; Weber, B. Improved *in vivo* two-photon imaging after blood replacement by perfluorocarbon. *J. Physiol.* **2009**, *587*, 3153-3158.
19. Maio, A.; Scaffaro, R.; Lentini, L.; Piccionello, A. P.; Pibiri, I. Perfluorocarbons-graphene oxide nanoplateforms as biocompatible oxygen reservoirs. *Chem. Eng. J.* **2018**, *334*, 54-65.

20. Sun, L.; Wang, L.; Tian, C.; Tan, T.; Xie, Y.; Shi, K.; Li, M.; Fu, H. Nitrogen-doped graphene with high nitrogen level via a one-step hydrothermal reaction of graphene oxide with urea for superior capacitive energy storage. *RSC Advances*. **2012**, 2 (10), 4498–4506.
21. Hetrick, E. M.; Schoenfisch, M. H. Analytical chemistry of nitric oxide. *Annu. Rev. Anal. Chem.* **2009**, 2, 409-33.
22. Ignarro, L. J.; Fukuto, J. M.; Griscavage, J. M.; Rogers, N. E.; Byrns, R. E. Oxidation of nitric oxide in aqueous solution to nitrite but not nitrate: Comparison with enzymatically formed nitric oxide from L-arginine. *Proc. Natl. Acad. Sci.* **1993**, 90, 8103-8107.
23. Nims, R.W.; Darbyshire, J. F.; Saavedra, J. E.; Christodoulou, D.; Hanbauer, I.; Cox, G. W.; Grisham, M. B.; Laval, F.; Cook, J. A.; Krishna, M. C.; Wink, D. A. Colorimetric methods for the determination of Nitric oxide concentration in neutral aqueous solutions. *A compansion to methods in Enzymology*. **1995**, 7, 48-54.
24. Balouiri, M.; Sadiki, M.; Ibnsouda, S. K. Methods for in vitro evaluating antimicrobial activity: A review. *J. Pharm. Anal.* **2016**, 6 (2), 71-79.
25. Diez-Pascual, A. M.; Diez-Vicente, A. L. Poly(propylene fumarate)/Polyethylene Glycol-Modified Graphene Oxide Nanocomposites for Tissue Engineering. *ACS Appl. Mater. Interfaces*. **2016**, 8 (28), 17902-14.
26. Siriviriyannun, A.; Imae, T.; Calderó, G.; Solans, C. Phototherapeutic functionality of biocompatible graphene oxide/dendrimer hybrids. *Colloids Surfaces B: Biointerfaces* **2014**, 121 469–473.
27. Ujihara, M.; Ahmed, M.M.M.; Imae, T.; Yamauchi, Y. Massive-exfoliation of magnetic graphene from acceptor-type GIC by long-chain alkyl amine. *J. Mater. Chem. A* **2014**, 2, 4244-4250.

28. Kebede, M. A.; Imae, T.; Sabrina; Wu, C. M.; Cheng, K. B. Cellulose fibers functionalized by metal nanoparticles stabilized in dendrimer for formaldehyde decomposition and antimicrobial activity. *Chem. Eng. J.* **2017**, *311*, 340-347.
29. Paulchamy, B.; Arthi, G.; Lignesh, B. D. A Simple Approach to Stepwise Synthesis of Graphene Oxide Nanomaterial. *J. Nanomed. Nanotechnol.* **2015**, *06* (01), 1-4.
30. Wang, C.; Feng, L.; Yang, H.; Xin, G.; Li, W.; Zheng, J.; Tian, W.; Li, X. Graphene oxide stabilized polyethylene glycol for heat storage. *Phys. Chem. Chem. Phys.* **2012**, *14* (38), 13233-8.
31. León, A.; Reuquen, P.; Garín, C.; Segura, R.; Vargas, P.; Zapata, P.; Orihuela, P. A. FTIR and Raman Characterization of TiO<sub>2</sub> Nanoparticles Coated with Polyethylene Glycol as Carrier for 2-Methoxyestradiol. *Appl. Sci.* **2017**, *7* (12), 49-58.
32. Kudin, K. N.; Ozbas, B.; Schniepp, H. C.; Prud'homme, R. K.; Aksay, I. A.; Car, R. Raman Spectra of Graphite Oxide and Functionalized Graphene Sheets. *Nano Lett.* **2008**, *8*, 36-41.
33. Yamini, D.; Venkatasubbu, G. D.; Kumar, J.; Ramakrishnan, V. Raman scattering studies on PEG functionalized hydroxyapatite nanoparticles. *Spectrochim. Acta. A Mol. Biomol. Spectrosc.* **2014**, *117*, 299-303.
34. Bukhtiyarov, A. V.; Kvon, R. I.; Nartova, A. V.; Prosvirin, I. P.; Bukhtiyarov, V. I. In-situ XPS investigation of nitric oxide adsorption on (111), (310), and (533) gold single crystal faces. *Surf. Sci.* **2012**, *606* (3-4), 559-563.
35. Ranke, W. UPS and XPS reference data of O, N, NO, (NO<sub>2</sub>)<sub>2</sub>, NH<sub>3</sub>, H<sub>2</sub>O, OH, H<sub>2</sub>S, SH and S on Ge surfaces. *J. Electron. Spectrosc. Relat. Phenom.* **1993**, *61*, 231-240.
36. Schairer, D. O.; Chouake, J. S.; Nosanchuk, J. D.; Friedman, A. J. The potential of nitric oxide releasing therapies as antimicrobial agents. *Virulence* **2012**, *3* (3), 271-9.



37. Cardozo, V. F.; Lancheros, C. A. C.; Narciso, A. M.; Valereto, E. C. S.; Kobayashi, R. K. T.; Seabra, A. B.; Nakazato, G. Evaluation of antibacterial activity of nitric oxide-releasing polymeric particles against *Staphylococcus aureus* and *Escherichia coli* from bovine mastitis. *Int. J. Pharm.* **2014**, *473* (1-2), 20-9.
38. Hetrick, E. M.; Shin, J. H.; Stasko, N. A.; Johnson, C. B.; Wespe, D. A.; Holmuhamedov, E.; Schoenfisch, M. H. Bactericidal Efficacy of Nitric Oxide-Releasing Silica Nanoparticles. *ACS Nano*. **2008**, *2*, 235–246.

## Graphical Abstract

